University of Stavanger

FACULTY OF SCIENCE AND TECHNOLOGY

MASTER'S THESIS

Study programme/specialisation: Mechanical and Structural Engineering and Material Science Specialization: Mechanical Engineering	Spring/ Autumn semester, 2020 Open / ~~Confidential~~
Author: Adrian Otter Falch Günther	
Programme coordinator: Knut Erik Giljarhus Supervisor(s): Knut Erik Giljarhus	
Title of master's thesis: Co-axial Propeller Configuration Optimization	
Credits: 30	
Keywords: UAV, Nordic Unnmanned, CFD, Co-Axial rotor setup, Low Reynolds, Axial Separation	Number of pages: 47 Stavanger, 29/06/2020 date/year

June 28, 2020

Abstract

The majority of research into Co-axial rotor setup involves same-sized propellers. Different-sized propellers have received less attention. The combination of low Reynolds number ($< 500\ 000$) and different-sized propellers even less.

This thesis is looking into co-axial propeller interference with various axial separation and effects concerning different-sized propellers in the co-axial setup, while operating in a small scale. The studies were conducting using Computational Fluid Dynamics simulations in the open-source software OpenFOAM.

Using a larger sized lower propeller than upper propeller lowers the lower propeller efficiency loss by avoiding upper propeller slipstream affecting essential lift areas on the lower propeller. Using efficiency as a measure of thrust per watts, the highest efficiency gain on lowest propeller was recorded using a combination of a small and large propeller, respectively 28" and 32" diameter propeller. However, the highest overall efficiency was found using both upper and lower propeller as the largest (32") propeller available, because of the increase in efficiency of all propellers when reducing rotational velocity.

The propeller axial separation study showed small variations on efficiency when the lower propeller is operating in the upper propeller's slipstream. This is because of an increased efficiency of upper propeller while the efficiency of lower propeller is decreased, with an increased axial separation. Only at very low axial separation values, the upper propeller had a significant loss of efficiency, which lead to an overall efficiency loss.

Preface

Finishing my Structural Engineering and Material Science degree at University of Stavanger has because of Nordic Unmanned's interesting problem proposal have been very enjoyable. First and foremost, I'd like to thank my supervisor at UiS, Knut Erik Giljarhus, for patience and guidance throughout the process. I'd also like to thank the bachelor group consisting of Stian Runestad Hidle and Vetle Byremo Ingebretsen, they have been providing interesting discussions, and data to help guide and validate my simulations. And lastley Aboma Wagari Gebisa at UIS 3D Lab, aiding me with 3D scanning.

Contents

List of Figures

List of Tables

Nomenclature

Acronyms

BEMT Blade Element Momentum Theory

CAD   Computer- Aided Design

CFD   Computational Fluid Dynamics

LSB   Laminar Separation Bubble

NACA National Advisory Committee for Aeronautics

NASA National Aeronautics and Space Administration

OpenFOAM Open source Field Operations and Manipulations

PISO Pressure Implicit with Splitting of Operator

RANS Reynolds-Average Navier Stokes

Re   Reynolds Number

RPM   Revolutions Per Minute

SA   Spalart Allmaras

SIMPLE Semi-Implicit Method for Pressure Linked Equations

UAV   Unmanned Aerial Vehicle

UiS   University of Stavanger

Other symbols

ρ Density

A Surface Area

C_d Drag Coefficient

C_l Lift Coefficient

F_D Drag Force

F_L Lift Force

g Gravitational Constant

Δs First Layer Thickness

Γ Diffusion coefficient

κ Compressibility coefficient

μ Dynamic viscosity

∂ Partial derivative

ϕ Generic flux

τ Shear Stress

u_τ Friction Velocity

c   Chord length

div   Divergence

divU   Volumetric deformation

grad   Gradient

k   Turbulent kinetic energy

L   Characteristic Length

l   Chord width

r   radius

U   Mean velocity in x direction

u   Instantaneous velocity in x direction

u'   Fluctuation velocity in x direction

V   Mean velocity in y direction

v   Instantaneous velocity in y direction

v'   Fluctuation velocity in y direction

W   Mean velocity in z direction

w   Instantaneous velocity in z direction

w'   Fluctuation velocity in z direction

y^+ Dimensionless quantity

Introduction

UAVs (Unmanned Aerial Vehicle), or more commonly known as drones, have over the last decade expanded rapidly in the civil market [1]. A lot of aerial tasks previously accomplished by a helicopter can in many cases easily be accomplished by a UAV optimized particularly for that task, and it it usually significantly cheaper and potentially faster. Nordic Unmanned is an example of a business that have commercially started to use UAVs. Their UAV service can include operations such as aerial inspection, photogrammetry, 3D-modeling of terrain and constructions, film and photo and thermographic imaging [2].

The size of the UAVs depends on the specific objective of the UAV. Nordic Unmanned uses UAVs in many different sizes, considered in this thesis is the Staaker BG-200, with a carry capacity of 25kg. Nordic Unmanned is using a coaxial propeller configuration to increased its octocopter's carry capacity. An overlapping propulsion system such as a coaxial octocopter provides one of the smallest platform volume per thrust output [3]. However the upper rotor outperforms the lower propeller because of the interference of the down-wash of the upper to the lower propeller. The combined rotor efficiency, in terms of upward thrust per power, of the coaxial rotor configuration is lower than a stand-alone single rotor configuration.

The use of coaxial rotor design in a helicopter, unlike the single rotor design, all the power is used for vertical thrust and the contra-rotating co-axial rotor configuration removes the need for the vertical tail rotor. The tail rotor cancels the yaw effect of the torque created by the rotation of the main propeller. The tail rotor shaft is estimated to consume 5-10 % of the total power, and the tail rotor is also one of the prime causes of helicopter accidents [4].

The benefits from canceling yaw in a co-axial rotor configuration on a helicopter is not required in a octocopter. Because of the additional propeller, the yaw effect can be canceled out by contra-rotating half the propellers. For any quad-, hexa, or octocopter, and so on, there is no need for a yaw canceling effect using a tail rotor. Nor does any UAV when using a coaxial

rotor setup.

A small scale UAV operates within a lower Reynolds number airflow than a manned helicopter, which operate in a high Reynolds number airflow (Re > 500,000). To accurately predict the performance of co axial rotors operating in low Reynolds air flows is a challenging task. There is high complexity of single propeller and co axial propeller airflow assessment, and serious problems related to boundary separation and transitions have been encountered at lower Re. Walker, at the Langley Research Center in Hampton studied a phenomenon called Laminar separation bubble, and found that the Eppler 387 airfoil is dominated by laminar separation bubbles at Reynolds numbers below 200 000 [5].

The turbulence model in this thesis is Spalart Allmaras. Spalart Allmaras is intended for fully turbulent high Reynolds number computations and is demonstrated to not predict relaminarization [6].

Looking at the combination of different sized propellers in a co-axial setup, Leishman and Anathan found that for a same sized propeller coaxial rotor setup outside the region affected by the slipstream, the blade thrust gradient values of the lower propeller recovers to values that are consistent with the upper rotor [7]. Increasing the diameter of lower propeller compared to the upper propeller can therefore potentially diminish the efficiency loss of the lower propeller.

Brazinskas et al looked at the co-axial separation and found that the axial separation effects the rotors efficiency differently [3]. At an axial separation of 0.60 z/D, the upper rotor operates similar or even more efficient to the performance of the single isolated rotor, while the lower rotor operates at the highest efficiency loss at the same axial separation. The lower rotor operates with the least efficiency loss around 0.05 z/D where the upper rotor has its highest efficiency loss.

Nordic Unmanned believes that one of the largest efficiency losses today is the coaxial propeller configuration, and they seek to optimize their propeller configuration. The scope of this thesis is to optimize the co-axial propeller configuration of Staaker BG-200 to extend flight endurance. This will be done using computational fluid dynamics, and by comparing the efficiency of proposed co axial propeller configuration against the efficiency of a standard propeller configuration currently used by Nordic Unmanned. Four different propellers commercially available is going to be tested, to determine what configuration provides the highest value0s of upward thrust per power usage. This thesis will also look at a few selected axial separation distances and how they effect the overall efficiency of the co-axial propeller configuration.

The general theory behind the equations and methods used in this thesis will be presented in chapter 2. Chapter 3 has case specific details and prepara-

tion of 3D models. This thesis is divided in terms of 2D- and 3D simulations, 2D simulations are used as validation for turbulence model and proposed grid structure. The 2D simulations are presented in chapter 4, while the 3D simulations and the results of the co-axial CFD simulations will be presented in chapter 5. Lastly, chapter 6 will conclude this thesis and present recommendation for further work.

Theory

This chapter will present the theory and governing equations in this thesis. Starting off with a simple introduction into aerodynamics and attempting to highlight a few key differences and similarities between a normal airplane wing and a rotating propeller. Followed by basic fluid dynamics concepts and how Reynolds Average Navier Stokes yields additional terms to the Navier Stokes equations to model turbulent flow. Lastly, how Finite Volume Method is used to to obtain an approximation of a solution to Reynold Averaged Navies Stoke partial differential equations.

2.1   Aerodynamics

In order to keep a object in air, lift generated by the plane needs to be larger than the gravitational forces acting on the plane. And to move a plane forward, the forward thrust need to be larger than the drag forces acting on the plane.
Lift is generated when the shape of the object is forcing the streamlines to curve around the object. In order to curve the streamlines its necessary with a pressure gradient, see equation 2.1.

$$\frac{\partial p}{\partial r} = \frac{\rho U^2}{r},$$ (2.1)

where r is the curve of the streamlines, U is the velocity. The pressure gradient acts as a centripetal force increasing the pressure-difference as velocity increases or curve of the streamlines decreases. For an airfoil, assuming atmospheric pressure far from the airfoil, this leads to a decreasing pressure on the upper surface of the airfoil and an increasing pressure on the lower surface of the airfoil. This pressure difference gives a total aerodynamic force which can be decomposed into lift- and drag force.
Many objects can generate lift and its not always considered a wanted effect.

Lift can be very problematic in instances such as formula 1- or speed boats racing, where keeping the vehicle attached to the surface is crucial. Although within aerodynamic, increased lift or upward thrust while minimizing drag is normally favored. The majority of the lift generated by an airplane is at the upper surface of the wing, and the wing shape is optimized in order to create a favorable lift/drag ratio [1]. Factors affecting lift and drag looking at the pressure gradient, can be shape and size, affecting the curvature of the streamlines. The motion, affecting the velocity of the streamlines or the fluid properties, affecting density. Additional considerations to a propeller is the inflow and outflow of the propeller, especially for a co axial rotor setup where the lower propeller is operating in the slipstream of the upper propeller. A propeller can be considered a rotating wing and the factors affecting lift of a propeller is the same as a wing. Because of the rotational motion, the wind velocity is changing along the leading edge of a propeller. While a plane wing has wind velocity at the wings equal to the velocity of the plane. Therefore, wind velocity refers to wind striking perpendicular to the leading edge of the wing, while rotational wind velocity refers to the wind striking perpendicular to the leading edge of a propeller.

Calculating lift- and drag force per unit length can be done using equations 2.1 and 2.3.

$$F_L = \frac{C_l \rho U^2 c}{2} \tag{2.2}$$

$$F_D = \frac{C_d \rho U^2 c}{2} \tag{2.3}$$

where, ρ is the density and c the length of the airfoil.

Notice that a coefficient for lift and drag is needed. These can be calculated by using a controlled environment where velocity, density and area are known, or numerically calculated. The Lift and drag coefficients combines several factors, such as shape and Angle of Attack. Angle of Attack or AoA is the angle between the direction of motion and the chord line of the airfoil. CFD simulations is an excellent way to numerically determine these coefficients.

Considering a propeller rotating in still air, the inflow generated by the rotating propeller combined with the rotational wind velocity results in the airflow the propeller actually operates in called relative rotational wind velocity. In this thesis, the air stream above the propeller affected by the rotating propeller is called the inflow. And the outflow, as the extension of the inflow after leaving the propeller. And Slipstream is the area below the propeller affected by the outflow.

airstream in negative z- direction of inflow is called induced flow, and affects

the direction of motion. AoA is effected by inflow by increased velocity of induced flow leads to a declined relative rotational wind direction, normally decreases the AoA. since AoA and the lift closely related,an increase of the magnitude of induced flow would lead to a decrease in lift because of the new relative rotational wind orientation decreased the AoA.

2.1.1 Co-axial

Co- axial propeller configuration is a configuration where a pair of propeller is operating, one above the other. Both propeller generate lift in the same way as an isolated propeller, but the resultant airflow is different dependent on interference between the lower and upper propeller. As mentioned in the introduction, co-axial propeller setup is beneficial for canceling the torque, normally created by a single rotor setup and removing the need for a vertical tail rotor. In addition to the inflow generated by the lower propeller in a coaxial setup, the lower propeller is also operating in the slipstream of the Upper propeller.

2.2 Fluid Dynamics

An important part of a solving fluid problem is to define physical phenomenon, fluid properties and to to specify appropriate boundary conditions. This is accomplished by determining whether the fluid is in-compressible/ Compressible, Newtonian/ Non-Newtonian and if it's a laminar/turbulent flow. Coefficient of compressibility is defined as; see equation 2.4.

$$\kappa = -\rho(\frac{\partial P}{\partial \rho})_T \tag{2.4}$$

A large value of κ indicates that a large change in pressure is needed to cause a small fraction change in volume. In most cases, especially at sea level and at low velocity, air is considered to be in-compressible. Most common fluids such as water, air, oil is are Newtonian, and the rate of deformation is proportional to the applied shear stress.
Laminar flow is a stable well ordered state of fluid flow in which all pairs of adjacent fluid layers move alongside one another and no intermixing of layers occurs. A flow that is not laminar is either turbulent or transitional to turbulent, which occurs above a critical Reynolds number [8].

2.2.1 Reynolds's Number

The Reynolds's number (Re) is a dimensionless value that describes the degree of laminar or turbulent flow. The Re along a flat plate can be calculated from:

$$Re = \frac{\text{Inertial Force}}{\text{Viscous Force}} \quad , \quad Re = \frac{\rho \; vl}{\mu} \tag{2.5}$$

where, v is the fluid velocity, l is chord width, ρ is density and μ is the dynamic viscosity of the fluid.

The Reynolds number tells that when viscous forces are less than inertial forces, the flow is turbulent, and when the inertial forces are less than the viscous forces, the flow is laminar. For a uniform free stream along a smooth flat plate the transition process towards turbulent flow start at critical Reynolds number, $Re_{crit} = 1x10^5$ and becomes fully turbulent when the $Re > 3x10^6$ [8].

When the fluid flow is either turbulent or in the transition process towards turbulent, a description of turbulent flow is needed. Reynolds-averaged Navier Stokes equations (or the RANS equations) is method used to achieve mathematical equations describing turbulence. The RANS equations is an modification of the Navier -Stokes equations.

Navier-Stokes equations

To explain RANS, its easiest to start with the Navier Stokes equations and see the effects of fluctuations on the mean flow. Navier stokes equations for an in-compressible flow with constant viscosity in a Cartesian co-ordinate system, see equations 2.6, 2.7, 2.8 and 2.9.

$$\text{div } \mathbf{u} = 0 \tag{2.6}$$

$$\frac{\partial u}{\partial t} + \text{ div}(u\mathbf{u}) = -\frac{1}{\rho}\frac{\partial p}{\partial x} + \nu \text{ div}(\text{grad}(u)) \tag{2.7}$$

$$\frac{\partial v}{\partial t} + \text{ div}(v\mathbf{u}) = -\frac{1}{\rho}\frac{\partial p}{\partial y} + \nu \text{ div}(\text{grad}(v)) \tag{2.8}$$

$$\frac{\partial w}{\partial t} + \text{ div}(w\mathbf{u}) = -\frac{1}{\rho}\frac{\partial p}{\partial z} + \nu \text{ div}(\text{grad}(w)) \tag{2.9}$$

The Navier Stokes equations flow variable u, is replaced by the sum of a mean and fluctuating component U and u'. Flow variable u is the x- component of the velocity vector $\mathbf{u}$ in this situation. Also the y- and z- component can be

replaced, thus table 2.2.1.

$$\mathbf{u} = \mathbf{U} + \mathbf{u'} \quad u = U + u' \quad v = V + v' \quad w = W + w' \quad p = P + p'$$

Replacing the flow variables in the instantaneous continuity and Navier-Stokes equations gives the equation set called Reynolds-averaged Navier-Stokes equations[9].

2.2.2 Turbulence modelling

To accurately calculate turbulence is very time consuming and costly, because of the complexity of the turbulent flow. RANS equations are time-averaged equations of motion used to describe a turbulent flow. There are several methods of describing turbulent flow, but this thesis will only present Reynolds- Averaged Navier Stokes equations.

Reynolds-averaged Navier-Stokes equations

Equation 2.10, 2.11, 2.12 and 2.13. shows the flow variables $\mathbf{u}$, u, v, w and ρ in the Navier Stokes equations replaced by the sum of a mean and fluctucating component as shown in table 2.2.1 .
Continuity

$$\text{div } \mathbf{U} = 0 \tag{2.10}$$

Reynolds Averaged Navier Stokes equations

$$\frac{\partial U}{\partial t} + \text{ div}(U\mathbf{U}) = -\frac{1}{\rho}\frac{\partial P}{\partial x} + \nu \text{ div}(\text{grad}(U))$$
$$+\frac{1}{\rho}\left[\frac{\partial(-\rho\overline{u'^2})}{\partial x} + \frac{\partial(-\rho\overline{u'v'})}{\partial y} + \frac{\partial(-\rho\overline{u'w'})}{\partial z}\right] \tag{2.11}$$

$$\frac{\partial V}{\partial t} + \text{ div}(V\mathbf{U}) = -\frac{1}{\rho}\frac{\partial P}{\partial y} + \nu \text{ div}(\text{grad}(V))$$
$$+\frac{1}{\rho}\left[\frac{\partial(-\rho\overline{u'v'})}{\partial x} + \frac{\partial(-\rho\overline{v'^2})}{\partial y} + \frac{\partial(-\rho\overline{v'w'})}{\partial z}\right] \tag{2.12}$$

$$\frac{\partial W}{\partial t} + \text{ div}(W\mathbf{U}) = -\frac{1}{\rho}\frac{\partial P}{\partial z} + \nu \text{ div}(\text{grad}(W))$$
$$+\frac{1}{\rho}\left[\frac{\partial(-\rho\overline{u'w'})}{\partial x} + \frac{\partial(-\rho\overline{v'w'})}{\partial y} + \frac{\partial(-\rho\overline{w'^2})}{\partial z}\right] \tag{2.13}$$

Comparing the Reynolds-average Navier Stokes equations with the Navier Stokes equations, on the right hand side there is additional terms. These new terms involve products of fluctuating velocities and are associated with convective momentum transfer due to turbulent eddies. They result from six additional turbulent stresses and are called the Reynolds stresses[9].

Reynolds stresses

Three normal stresses

$$\tau_{xx} = -\rho\overline{u'^2} \qquad \tau_{yy} = -\rho\overline{v'^2} \qquad \tau_{zz} = -\rho\overline{w'^2} \tag{2.14}$$

and three shear stresses.

$$\tau_{xy} = \tau_{yx} = -\rho\overline{u'v'} \qquad \tau_{xz} = \tau_{zx} - \rho\overline{u'w'} \qquad \tau_{yz} = \tau_{zy} - \rho\overline{v'w'} \tag{2.15}$$

In order to be able to compute turbulent flows with the RANS equations a turbulence model is required to calculate the Reynolds stresses. The Spalart Allmaras is an example of a turbulence model, and is developed specifically for aerodynamic flows.

2.2.3 Spalart Allmaras - SA

Spalart Allmaras is a one-equation RANS turbulence model. It was developed for aerodynamic flows, since the previous k epsilon model and did not solve the boundary layer well enough . The model uses the Boussinesq equation to calculate the Reynolds stresses[10]. The general SA model is a linear eddy viscosity model, and the eddy viscosity is related to $\tilde{\nu}$ by

$$\mu_t = \rho\tilde{\nu}f_{v1} \tag{2.16}$$

$$\underbrace{\frac{\partial(\rho\tilde{\nu})}{\partial t} + \text{div}(\rho\tilde{\nu}\mathbf{U})}_{\textbf{Advection}} = \underbrace{\frac{1}{\sigma_\nu}\text{div}\left[(\mu + \rho\tilde{\nu})\text{grad}(\tilde{\nu}) + \text{C}_{b2}\rho\frac{\partial\tilde{\nu}}{\partial x_k}\frac{\partial\tilde{\nu}}{\partial x_k}\right]}_{\textbf{Diffusion}}$$

$$+ \underbrace{\text{C}_{b1}\rho\tilde{\nu}\tilde{\Omega}}_{\textbf{Production}} - \underbrace{\text{C}_{w1}\rho\left(\frac{\tilde{\nu}}{\kappa y}\right)^2 f_w}_{\textbf{Dissipation}} \tag{2.17}$$

$$\tilde{\Omega} = \Omega + \frac{\tilde{\nu}}{(\kappa y)^2}f_{\nu 2}$$

where

$$\Omega = \sqrt{2\Omega_{ij}\Omega_{ij}} \quad = \text{mean vorticity}$$

and

$$\Omega_{ij} = \frac{1}{2}\left(\frac{\partial U_i}{\partial x_j} - \frac{\partial U_j}{\partial x_i}\right) \quad = \text{mean vorticity tensor}$$

The functions

$$f_{v1} = f_{v1}(\frac{\tilde{\nu}}{\nu})$$

,

$$f_{v2} = f_{v2}(\frac{\tilde{\nu}}{\nu})$$

and

$$f_w = f_w(\frac{\tilde{\nu}}{\tilde{\Omega}\kappa^2 y^2})$$

are wall damping functions. model constants

$$\sigma_v = \frac{2}{3} \quad \kappa = 0.4187 \quad C_{b1} = 0.1355 \quad C_{b2} = 0.622 \quad C_{w1} = C_{b1} + \kappa^2\frac{1+C_{b2}}{\sigma_v}$$

These model constants have been tuned for external aerodynamics flows. The use of a turbulence model such as Spalart Allmaras in a low Reynolds number airflow over a airfoil or propellers requires high level of refinement close to the wall of the airfoil[10]. Model and model constants have been shown to give good performance in the presence of adverse pressure gradients [9]. Adverse pressure gradient is an unfavorable pressure gradient and is main attribute for boundary layer separation.

2.2.4 Laminar Separation Bubble

An interesting phenomena of boundary layer separation and reattachment can occur on a airfoil operating in low Reynolds's number flow, called Laminar Separation bubble. The presence of a adverse pressure gradient causes the separation of the boundary layer, and the flow to transition from laminar to turbulent flow. In an high Reynolds's number flow, after separation the airflow stays fully turbulent across the airfoil, but in a low Reynolds's number flow the turbulent flow can touch the surface and reattach, forming a Laminar Separation bubble. The volume enclosed by the separated laminar and turbulent flow have almost none energy exchange with the outer flow, reducing the overall lift and drag of the wing[11].

2.3 Computational Fluid Dynamics

Computational Fluid Dynamics or CFD, is a computer-based simulations and analysis of a systems involving fluid flow, by the means of computer-based simulations. An example of one of the industries utilizing this technique is industries concerning aerodynamics of aircraft and vehicles. Formula 1 wanting to reducing drag or/and increase downforce (reversed lift, spoiler), commercial airplanes minimizing costs or the military increasing flight length of their missiles. Some of the benefits using CFD is substantially reduction of costs of new design, study systems without risk concerning hazardous condition or pushing systems beyond their capacity without the costs of accidents scenarios. Most commercial CFD packages contain three main elements, pre- processor, a solver and post processing. The pre –processor consists of defining the computational domain, creating a grid with a satisfactory grid quality, specify fluid properties and boundary conditions. Finite volume method is a numerical solution technique used in the most well established CFD codes and used as the solver element of this thesis. The last element of CFD packages is post processing and used to presents the results from the simulations [9].

2.3.1 Finite Volume Method

Finite Volume Method, or FVM, is a common method used in CFD to solve complex fluid partial differential equations numerically. Rewriting the Navier stokes equation 2.7 in integral form over a control volume gives the steady transport equation:

$$\int_A \mathbf{n}.(\rho\phi\mathbf{u})dA = \int_A \mathbf{n}.(\Gamma \text{ grad } \phi)dA + \int_{CV} S_\phi dV \qquad (2.18)$$

where the first term is the convection term, second is diffusion, last term is the source term and $\mathbf{n}$. is the vector normal to the surface element dA. The integration of the partial differential equations generates a statement of the conservation of a fluid property such as 1, u, v, w, and i, for a finite size [9] . A finite size in computational dynamics refers to the small volume surrounding each node point in a mesh, or each cell. Using the Gauss theorem, converting the volume integral into a surface integral and in the absence of sources, the one dimensional steady convection and diffusion of a property ϕ is used as an example of solution applying FVM, and is given as:

$$\frac{d}{dx}(\rho u\phi) = \frac{d}{dx}\left(\Gamma\frac{d\phi}{dx}\right) \qquad (2.19)$$

which must satisfy continuity, so $\frac{d(\rho u)}{dx} = 0$. Integrating the transport equation focused on a general node P; with neighbouring control volume faces w and e:

$$(\rho u A \phi)_e - (\rho u A \phi)_w = \left(\Gamma A \frac{d\phi}{dx}\right)_e - \left(\Gamma A \frac{d\phi}{dx}\right)_w \qquad (2.20)$$

With continuity integrated as, $(\rho u A)_e - (\rho u A)_w = 0$, let variable F and D represent the convective mass flux per unit area and diffusion conductance at cell faces. The integrated convection - diffusion equation can be rewritten as:

$$F_e \phi_e - F_w \phi_w = D_e(\phi_E - \phi_P) - D_w(\phi_P - \phi_W) \qquad (2.21)$$

And integrated continuity equation as $F_e - F_w = 0$. Discretiazation schemes can be used in order to calculate the transported property ϕ at the e and w faces[9].

2.3.2 Discretiazation Schemes

Utilizing FVM as method for solving CFD simulations, requires discretisation schemes to calculate the transport properties ϕ_e and ϕ_w. The most common discretisation schemes, and used in this thesis, is the Central differencing scheme and Upwind differencing scheme.
Central differencing scheme seems to yield accurate results when the F/D ratio is low, and the convection- diffusen problems takes the same general form as for pure diffusion. Central differencing schemes are usually an effective choice of gradient scheme. Upwind Differencing schemes is beneficial when the flow becomes strongly convective because the direction is taken into account [12].

2.3.3 SIMPLE- and PIMPLE algorithm

The most popular solution algorithms for pressure and velocity calculations is SIMPLE, which is an iterative procedure for calculation of pressure and velocity fields. Suited for steady state, incompressible and turbulent flow. SIMPLE stands for Semi- Implicit Method for Pressure Linked Equations and is basically a guess and correct solver, and starting from an initial pressure field guess p*. Then solving the discretised momentum equations to compute the intermediate velocity field, solving the pressure correction equations, correcting the pressure and velocities, solving all other discretised transport equations and finally see if the pressure-, and velocity corrections will all be

zero in a converged solution. If not, the Simple Algorithm set p* = p, u* = u, v* = v and ϕ* = ϕ and repeat until the solution has converged or reached preferred tolerance [9]. In this thesis, a dynamic mesh will be introduced in order to simulate rotating propellers. Since Simple is a steady state solver, a transient solver must be introduced.

PIMPLE algorithm is a combination of PISO and SIMPLE, where PISO (Pressure Implicit with Splitting of Operators) has a further corrector step to SIMPLE. PIMPLE is a transient solver for incompressible, turbulent flow of a Newtonian fluid, suited for a moving mesh. Pimple solves the equation of momentum equal to the one in SIMPLE, except that time differential is used for calculation sphere. Can be thought of as a SIMPLE solver for each time step, and once converged, the solver will move on to the next time step.

2.3.4   Grid generation

Grid generation is a major part of the pre processsor element of most CFD packages. The accuracy of a CFD solution is hugely affected by the number of cells in the grid. A finer grid tends to provide more accurate solution, but at an increasingly computational cost. Optimal meshes are finer in areas of large variations and coarser in areas of little change. Presently it's up to the CFD user to design a grid that is suitable for the given case [9].

The far field boundaries are fairly easy to determine in a external flow field, but the increased cell refinement around model surface can be more difficult to determine. Y+ is a none dimensional distance representing the distance from a model surface to the first cell node, takes into account the fluid motion, properties, geometry and friction of the wall, and can be used to determine the highest level of refinement needed in a mesh. In order to generate an optimal mesh, using the first layer height calculated using an appropriate y+ value and smooth transition into the background mesh can provide a low computational mesh still providing high accuracy simulations.

Surface Layer

In order to calculate y+ at a flat plate, use Reynolds's Number calculated from equation 2.5 to determine the friction coefficient at the wall. For a smooth surface, use equation 2.22.

$$C_f = \frac{0.026}{Re_x^{1/7}} \tag{2.22}$$

Knowing the friction coefficient, equation 2.23 is used to calculate the wall shear stress, where U_∞ is the free air stream velocity.

$$\tau_{wall} = \frac{C_f \rho U_\infty^2}{2} \tag{2.23}$$

Using the wall shear stress, equation 2.24 is used to calculate the friction velocity used in equation 2.25. Use equation 2.25 to calculate the first layer height using an appropriate y+ value.

$$U_{fric} = \sqrt{\frac{\tau_{wall}}{\rho}} \tag{2.24}$$

$$\Delta s = \frac{y^+ \mu}{U_{fric} \rho} \tag{2.25}$$

In aerodynamics and airfoils operating in transitional or turbulent flow, the occurrence of adverse pressure gradients, requires the first layer height to be within the viscous sub-layer. A reasonable y+ value using the Spalart Allmaras turbulence model is y+ of less than 1 [13].

2.3.5   OpenFOAM

OpenFOAM stand for Open source Field Operation And Manipulation. OpenFOAM being a Open source CFD toolkit allows the user to freely use and modify a high-end CFD code. OpenFOAM is operated from the terminal window and written in C++.

With the absence of an integrated graphical user interface, OpenFOAM is a folder based toolkit and consist of three main directories, constant, system and 0 [14].

STAAKER BG-200

2 master students performing computerized optimization, and a bachelor group performing optimizations experimentally at UiS machine labratory is working on the same octocopter, the Staaker BG-200 by Nordic Unmanned see figure 3.1. The experimental data is available, and it is used to validate and to see agreements with results provided by CFD simulations in this thesis. This chapter will try to provide all case specific data used in the following chapters with focus on optimizing the coaxial rotor configurations.

3.1 System Description

As seen in figure 3.1 the BG-200 is a coaxial octocopter. The standard propeller configuration setup is using 28"x9.2" propellers both as upper and lower propeller with an axial separation of 109.2 mm.
According to Unmanned Nordic, the BG-200 has a max takeoff weight of 25 kg. While minimum flying weight is 16 kg (8.5 kg drone and 7.5 kg battery). The flight endurance plot, see BG-200 Technical Sheet, using the standard 32 Ah batteries states a theoretical maximum flight endurance of 60 min without payload [15]. Among other ways to increase endurance of the Staaker, this thesis is focused around the propeller configuration.

3.1.1 Propeller Configuration

As mentioned, the Staaker is a co axial octocopter, using four co-axial rotor setups of two G28" x 9.2 propellers. The diameter and pitch of the propeller is respectively 711.2 mm and 233.7 mm. Pitch is described as a units of distance per rotation. And in this case, the propeller moves 233.7 mm upwards in one horizontal rotation. Three additional propellers are available. The G29"x9.5,

Figure 3.1: Staaker BG-200

Table 3.1: Propeller

Name	Diameter	Pitch
G28"x9.2"	28"	9.2"
G29"x9.5"	29"	9.5"
G30"x10.5"	30"	10.5"
G32"x11"	32"	11"

G30"x10.5 and G32"x11. G stands for glossy, and the remaining numbers
are diameter and pitch in inches. See table 3.1 for information about the
available propellers.

Reverse Engineering propellers

Free form reverse engineering is used in order to do simulations with these
propellers. According to M.P. Groover, Reverse engineering provides a means
by which three-dimensional data can be captured in a computerized form
from a physical object. And can be divided into two phases, digital docu-
menting and 3D modeling[16].

All four propellers were digitally documented using Creaform's Handyscan
3D (700) which is a handheld triangulation scanner. Triangulation 3D scan-
ners use either a line or a point to estimate data point coordinates on the
surface of the object. Triangulation scanner is not to be confused with a
triangulation mesh. The triangulation of the 3D scanner refers to the point
on the object, location of the laser diode and location of the camera. Trian-

Table 3.2: 3D modelled Propeller

Name	filetype	Diameter	Pitch	AoA
G28 9.2 CW	.stl	710 mm	234 mm	11,9°
G28 9.2 CCW	.stl	710 mm	234 mm	11,9°
G29 9.5 CW	.stl	734 mm	241 mm	11,9°
G29 9.5 CCW	.stl	734 mm	241 mm	11,9°
G30 10.5 CW	.stl	762 mm	267 mm	12,3°
G30 10.5 CCW	.stl	762 mm	267 mm	12,3°
G32 11 CW	.stl	816 mm	279 mm	12,7°
G32 11 CCW	.stl	816 mm	279 mm	12,7°

gulation scanners will not be explained any further in this thesis.

The digital documenting phase provides millions of data point coordinate creating a point cloud. Using Handyscan 3D with the connected software, VX elements creates a triangular mesh as it collects data point coordinates. According to Creaform the Handyscan 3D creates triangular mesh with an 0.025 mm accuracy [17], but because of the usage of red laser diode and its limitations to scanning black and glossy surfaces further refinement is required to create accurate and smooth propellers for simulations.

Instead of measuring the propellers, the data triangulation mesh created in the digital documenting phase provides a huge number of data points useful to accurately trace and reconstruct the propellers digitally. The propellers were divided ten times from hub to wingtip using Autodesk Inventor. Points along the cross section was selected in order to create an airfoil using an interpolation curve. The digital documenting phase had some problems accurately describing both leading- and trailing edge and an interpolation curve gives a more accurate interpretation of the curve at both edges. In order to reconnect all the cross sections, loft function was used. Two guidelines along the leading- and trailing edge were set as rails for the loft function. Since the cross section from hub to wingtip only creates one side of the propeller, the half propeller was copied and rotated 180 degrees along the z axis, assuming the propeller was places in the xy plane with origin in the center of the hub. The digitally created propellers were exported into a file type OpenFoam can recognize. For simplicity, ASCII STL file type was used. See Table 3.2 for all the reversed engineered propellers.

In table 3.2, CW and CCW stand for clockwise and counterclockwise and refers to the rotational direction of the propeller. Since the co axial setup is contra rotating, mirrored version of each propeller is made and named CCW. Also an averaged AoA is listed, the averaged values are taken from end of

hub to wingtip.

Axial Separation

The axial separation of the standard co-axial rotor setup is 109.2mm. Minimum axial separation is 91.2 with integrated rotors and maximum 149.2 using quick connections for the propellers.

3.1.2 Flight Conditions

Nordic Unmanned calculated their Staaker BG -200 to have a flight endurance of 60 min with a weight of 16 kg, no payload [15]. The combined thrust of all propellers needs to counteract this weight to stand still in air, this is called hovering. The experimental data collected at UiS laboratory provided data such as, gram force (gf) as an indication of vertical thrust, rotational speed as rounds per minute (RPM), and torque in Newton meter and various information indicating battery and power usage.

Table 3.3 is created by experimental data from UiS machine laboratory and shows the four propellers and standard co axial propeller setup with the RPM, and torque at vertical thrust closes to 4000-gram force (39.2 N) measured. Each co-axial propeller setup needs to provide vertical thrust equal to one fourth of the combined vertical thrust in order to hover (16 kg), and all single rotor propeller in table 3.3 have been adjusted in order to contribute with 0.60 of combined thrust (39.2 N) giving a better indication of upper propeller contribution of a co axial setup at hover.

Table 3.3: Rotor Configuration - 40 N

Co-Axial	Thrust [N]	Torque [Nm]	RPM	Contrib
G28" 9.2"/G29" 9.2"				
Upper	25.2	0.895	2073	0.63
lower	15.0	0.731	2077	0.27
Single Rotor	**Thrust [N]**	**Torque [Nm]**	**RPM**	**Contrib**
G28" 9.2"	24.3	0.811	2027	0.60
G29" 9.5"	24.5	0.851	1862	0.60
G30" 10.5"	23.4	0.855	1634	0.60
G32" 11"	24.2	0.927	1510	0.60

Table 3.4: R_e across propeller blade

Propeller	G28 9.2 2000	G29 9.5 1900	G30 10.5 1600	G32 11 1500
L_b/x	R_e	R_e	R_e	R_e
0.4	141,422	148,468	131,308	139,851
0.5	164,150	173,557	151,863	162,567
0.6	175,767	188,318	161,758	175,209
0.7	176,777	195,525	164,031	177,657
0.8	173,746	189,143	154,769	175,973
0.9	154,554	168,502	130,154	159,835
Average	**164,000**	**177,000**	**149,000**	**165,000**

Reynolds's Number

To determine flight condition of the octocopter, Reynolds's Number can be used to determine the flow condition of the diverted free stream across the propeller blade. Reynolds's number can be calculated from surface area, density, kinematic viscosity and velocity as seen in equation 2.5.

Velocity can be calculated using the RPMs given in table 3.3, chord line can be measured from the 3D models of the propellers mentioned in table 3.2. And kinematic viscosity at standard atmospheric conditions, calculated R_e values in table 3.4. The cross sections is diveded ten times from gub to wing tip, L_b/x indicates the location of the corsssection along the blade length, 0 being hub and 1 being wing tip. Only values that has an airfoil shape is considered in table.

Table 3.4 shows R_e values at lowest possible rotational velocity for each propeller, barely hoovering, and according to the experimental data clearly indicates that the BG-200 operates within the low Reynolds's number flow.

Since the propeller operate within laminar, transitional and turbulent flow, it's needed a turbulence model to solve for the fluctuations. A 2D validation case will be performed in next chapter to choose the correct turbulence model and grid refinement levels along the boundaries. How to find a suitable CFD system to test all different option previously mentioned in this chapter can be a challenging task. To minimize the number of steps the NASA Langley research center has a turbulence modeling resource with the objective to provide resource for CFD developers to obtain accurate and up to date information on RANS turbulence models and to verify that models are implemented correctly. This thesis will use this resource to validate the choice of turbulence model along with a grid convergence study.

Simulation of 2D Airfoil

The purpose of this chapter is to perform a turbulence model- and grid generation validation for Open Foam's implementation of the turbulence model Spalart Allmaras, using the NASA Turbulence Modeling Resource. The NASA turbulence modeling resource will be used to establish that the model is implemented correctly.

4.1 Validation Case 2D

The case depicts at an airfoil operating in a velocity field of Reynolds number 1.52 million with an Angle of attack of 13.87 degrees, velocity at 27.13 m/s and kinematic viscosity $\mu = 0.1605\frac{cm^2}{s}$. The airfoil chord length was 90.12 cm. Experimental data provided by the turbulence model resource is the NACA 4412 surface pressure coefficients compiled in a .dat file and will be used to compare the obtained simulations results with the experimental data [18]. The turbulence modeling recourse also provide data of expected results using a range of different turbulence models. Expected results using the same turbulence model, Spalart Allmaras is;

- CL=1.7210, CD=0.02861

- CL=1.7170, CD=0.02947

Where C_l and C_d is the coefficients of lift and drag, values are SA results from two independent CFD codes, CFL32 and FUN32 [19].
The CFD simulations at the turbulence modeling resource implement the same initial conditions, but with an increased far field outer boundary, which is set to extend hundred times the chord line. This is far more than the relatively small wind tunnel used to obtain the experimental data.
This 2D simulations will be used in order to verify the choice of turbulence model, but also provide a way to determine level of grid refinement needed in order to minimize computational time whilst still providing accurate results.

4.1.1 Computational Setup

Geometry and Grid Generation

Creating a high-quality mesh is case specific. For an airfoil with adverse pressure gradients, a fine refinement along the airfoil is needed. This is usually accomplished by surface layer with start width of cell calculated to give a y+ < 1. The outer boundaries should not in any way affect the airflow around the airfoil and should therefore be far away from the airfoil. The grid created and used in the turbulence modeling resource had far field boundaries exceeding 100 times chord line, but the experimental tunnel was relatively small.

This 2D case will have a grid of 25 m in both x and y direction to minimize the effect of the boundaries as the initial grid. The boundaries are created and named in blockMeshDict. BlockMeshDict is needed when using snappyHexMesh. SnappyhexMesh is used to create the surface layers needed to obtain an y+ < 1 and all the other refinement levels. In blockMeshDict the first refinement level, level 0 is selected by choosing how many cells blockmesh should create along the length of x, y and z. The lowest refinement should be relative coarse, but determines how many refinement levels are needed to get a smooth transition from the last surface layer to rest of the mesh, preferably between 1.2 and 2. Where 2 is the expansion ratio from a higher refinement level to the lower, and 1.2 is the expansion ratio used between each surface layer.

After creating blockMeshDict, a calculation of minimum wall spacing which corresponds to y+ < 1, which is recommended for a incompressible- , turbulent flow in presence of adverse pressure gradients according to the theory under Surface Layer.

In chapter Theory, y+ can be calculated using equations 2.22, 2.23, 2.24 and 2.25. Calculating wall spacing of 1.324e-5 m to achieve a y+ < 1 and with a Reynolds number at 1.6e+6 at standard atmospheric conditions.

Using the know wall spacing of the first layer, and the outer boundary conditions, the number of refinement levels needed for a smooth transition can be calculated knowing the decreasing grid refinement level expansion ratio at 2. All data concerning the initial grid are given in table 4.1

Figure 4.1.1 shows five refinement levels and the increasing refinement level as the cells come closer to the airfoil. Purpose of the grid refinement is to increased refinement level in areas where the variables change and minimize the computational costs in area of little to none chance, such as the velocity and pressure changes along the airfoil requires an increased level of grid refinement. Looking at figure 4.1.1, the refinement airfoil three surface

Table 4.1: Initial Grid Calculations

Domain Thickness	25 m
Refinement level 0 thickness	0.25 m
y+, calculated first layer thickness	1.437 e-5 m
Highest refinement level	8
Highest refinement level thickness	9.766e-4 m
Relative size parameter	0.7
Final Layer thickness	6.835 e-4 m
Expansion ratio	1.3
Number of Surface Layer	16
First Layer thickness	1.335 e-5 m

refinement level along the five grid refinement levels creates a total of eight refinement levels as calculated in table 4.1. In addition figure 4.1.1 also visualize the surface layer refinement layers. 16 surface layers with increasing size, from first layer height providing an y+ < 1, providing a smooth transition into the highest surface refinement level of 8.
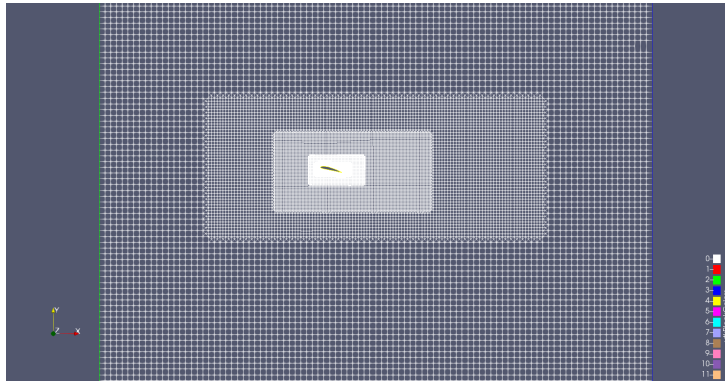

Figure 4.1: Grid

Solver Setting

An appropriate solver for an incompressible, turbulent flow is the SIMPLE algorithm as mentioned in Theory. SIMPLE is a steady state solver and appropriate for an external flow over a 2D Airfoil.
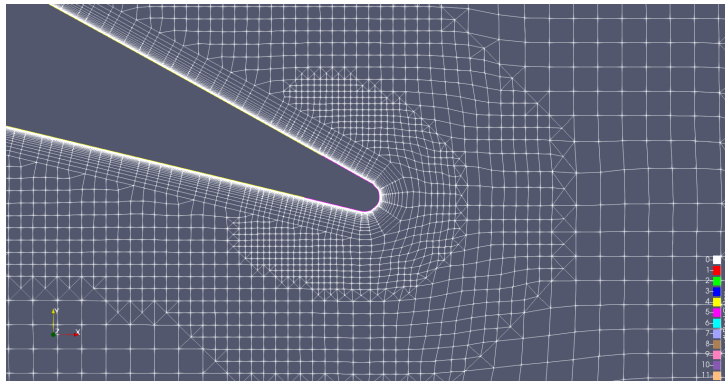
Figure 4.2: Surface Layer

4.1.2 Results of the 2D airfoil simulations

The initial grid calculations and solver setting shows that the steps used to do an initial good guess proves a fairly accurate result. Figure 4.1.2 show the pressure coefficient along the chamber line both for the experimental values provided by the NASA turbulence model resources and CFD simulation using the initial grid and solver settings.
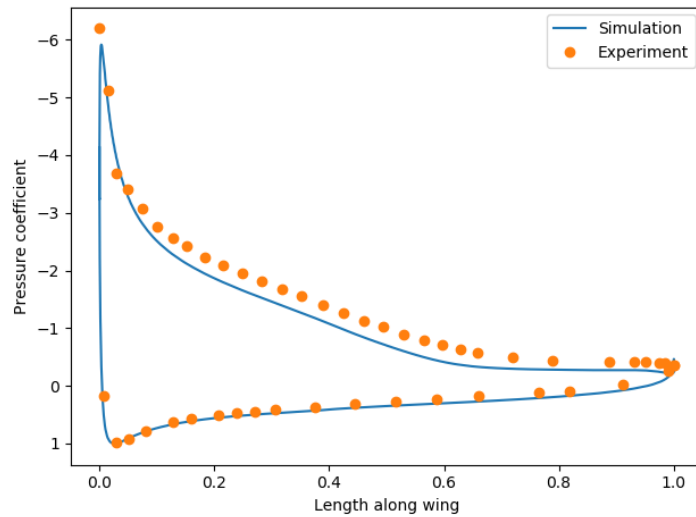

Figure 4.3: Coefficient of pressure over length along the wing

Figure 4.1.2 shows the residuals plotted against the iterations. After 3000 iterations, most residuals has a value of less than 10^{-4}. When changing the initial grid size in attempt to lower computational time, should pay attention

the the residuals even as they converge to a convergence tolerance of 10^{-4} they don't fall monotonically.
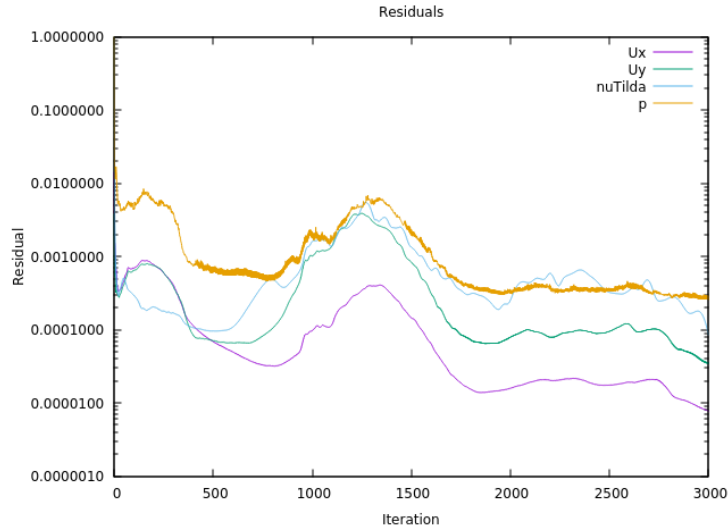

Figure 4.4: Residuals vs Iterations

Table 4.2 compares the coefficient for drag and lift between the initial simulation results and the expected values provided by the NASA turbulence modeling resource. The initial Simulation also has a y+ average of 0.467 at the trailing edge, fully developed surface layer thickness and a computational time of 316 seconds.

Table 4.2: Initial simulation

Values	Initial Simulation	Expected SSA Results	Error [%]
C_l	1.7811	1.7210, 1.7170	3.5, 3.7
C_d	0.0574	0.0286, 0.0295	200.7, 194.6

Initial simulation provides highly accurate values for lift coefficient, but clearly overestimates the drag coefficient, and drag is more than doubled when looking at equation 2.3 for calculating drag.

Gird Independence study

Preforming a gird Independence study can highlight when result are not negatively altered by a less optimal grid. Considering 3D simulation of a co-axial rotor setup, minimizing the computational time, while still providing accurate result, can be achieved doing a gird independence study. Since the

surface layer are relative to the highest surface refinement level. All cells are affected by changing the cell size of cells in refinement level 0. These cell sizes can be altered in blockMesh.

When comparing the different simulations in this grid independence study,a fully developed surface layer, and y+ < 1 is a requirement. While a minimal error percentage at minimal computational time will be weighted against each other. Table 4.3 shows the results from the grid Independence simulations. The simulations are named according to the number of cells of the simulation compared to the number of cells in the initial simulation in x, or y direction in blockMesh.

Table 4.3: Grid Independence

Values	Exp. SSA	0.5	0.75	InitialS	2
y+ at Wing Edge	< 1	28.423	0.4931	0.4670	0.4693
y+ at Wing	< 1	0.4701	0.4021	0.3868	0.3857
Surface Layer development		98.6	100	100	100
C_l	1.7210, 1.7170	1.726	1.753	1.7811	1.776
C_d	0.0286, 0.0295	0.057	0.0622	0.0574	0.0557
nCells		31,172	59,221	93,338	123,338
Computational Time [s]		99	196	316	442

Looking at table 4.3, all simulations provides results with very similar error % . 0.5 simulation does not pass the preset requirements of y+ have fully developed surface layer thickness. Simulation 2 is not fully a two times initial simulation, but a domain size increase. This is done to verify that the far boundaries doesn't interfere with the simulations results. Figure 4.1.2 and 4.1.2 shows the pressure coefficient along the chord line and residuals of simulation 0.75.

Laminar Separation Bubble

2D Validation case used in this thesis doesn't consider low Reynolds's number flow. Knowing the turbulence model Spalart Allmaras doesn't predict reattachment after boundary separation, the flow is considered fully turbulent.This leaves the validation of turbulence model; Spalart Allmaras with a crucial flaw. In an attempt to verify Spalart Allmaras as a turbulence model valid even for low Reynolds's number flow. A simplified study comparing results of Morgrado et al [11] looking into the development of Laminar Separation bubbles. Study on the E387 airfoil will be performed, testing different AoA and their development of laminar separation bubble.
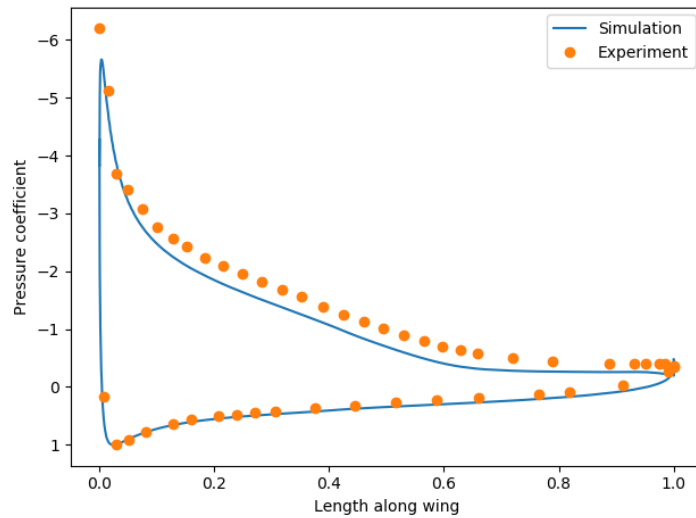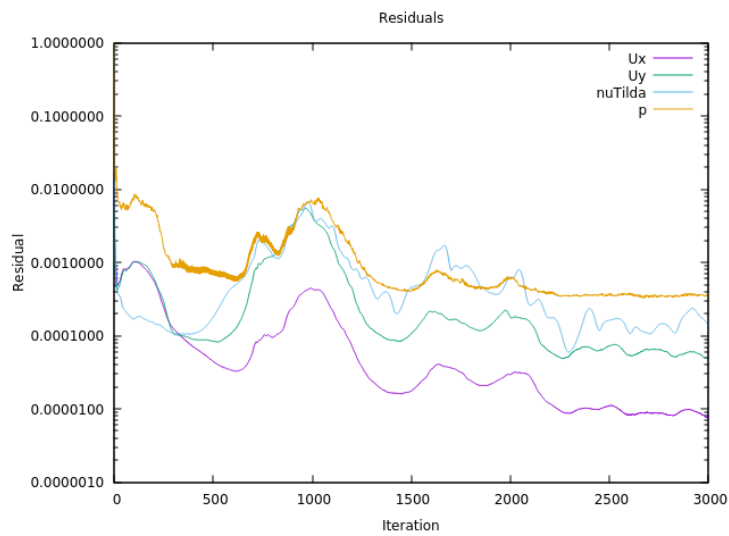
Figure 4.5: Pressure Along Chamber line

Figure 4.6: Residuals vs Iterations

The tests where accomplished using airfoil 387 at a velocity of 3 m/s at standard atmospheric conditions, which provides a Reynolds's Number flow of about 200,000, a lot closer to the case specific conditions mentioned in table 3.4.

Looking at figure 4.1.2, the experimental values clearly shows the development of a laminar separation bubble starting at 0.4 to 0.6 along the chamber

line of the airfoil. The simulation values register no such phenomena and for a airfoil operating in low Reynolds's number flow at four degrees angle of attack the overall lift and drag will be higher than experimental values. For figure 4.1.2 neither the simulation or the experimental data has any indication of the development of LSB and the flow is fully turbulent after separation.

Morgado et al studied modifications on the Spalart Allmaras model and other models considering the development of laminar separation bubbles [11].
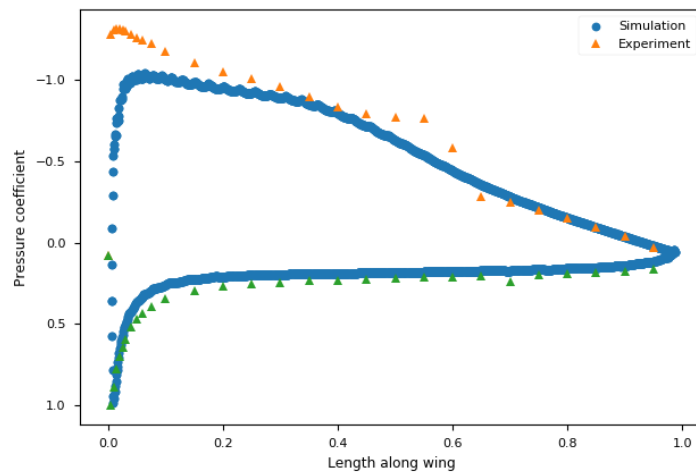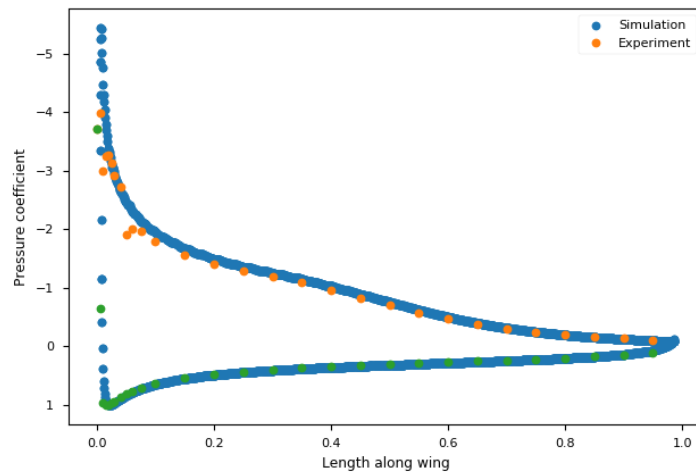

Figure 4.7: C_p Along Chamber line, 4 AoA

Figure 4.8: C_p Along Chamber line, 10 AoA

4.1.3   Discussion 2D Validation Case

Given by the turbulence modeling resource was experimental data and ex-
pected results using Spalart Allmaras as turbulence model. The experimental
data showed high accuracy, with a slightly overestimated pressure coefficient
as seen in figure 4.1.2 with CFD simulations using the initial grid. Compar-
ing with the expected results of the Spalart Allmaras as turbulence model,
gave highly accurate coefficient of lift, but a poor values of coefficient of
drag. Calculating drag using equation 2.3 shows an almost doubled drag
force acting on the wing, than what the expected value would suggest. The
accurate pressure field would suggest a more accurate ratio of lift and drag,
but the grid Independence study shows minimal improvements to drag coef-
ficient when increasing or decreasing mesh refinement.

Further study into solver settings and discretisation schemes could improve
accuracy, but knowledge of the need of a transient solver for the dynamic
mesh which will be used in the 3D simulations diminish the potential alter-
ing schemes and solver for this 2D simulation case. Overall, Spalart Allmaras
proves highly accurate, considering pressure field around the airfoil and lift
values. And the grid independent study shows that the accuracy is grid in-
dependent.

The validation case of turbulence model and grid independence study is done
using a validation case operating in high Reynolds's Number flow, unlike the
small scale UAV operating in low Reynolds's Number flow ,see 2.5, of focus
in this thesis.

An important difference when operating in low R_e flow is the development
of LSB. A small study of airfoil E387 shows the clear development of LSB
of airfoils operating in low R_e flow when AoA is relative small. Looking
at table 3.2 an average AoA ranging from 11.9° to 12.7° for the 3D mod-
elled propellers suggest the flow across the airfoil being fully turbulent after
boundary separation. Areas of the wing close to hub will suffer, lift wise,
the development of LSB. These areas is Low lift distribution areas, and no
modification to Spalart Allmaras will be implemented.

4.1.4   Conclusion 2D Validation Case

After reviewing the high overall accuracy and overestimated drag coefficient
of Spalart Allmaras as turbulence model. The choice of turbulence model
stays as is, and Spalart Allmaras will be used as turbulence model for the 3D
simulation of Single- and Co-axial rotor. Further, the initial grid calculation
will be similar in both cases demanding an independent grid independent
study for the 3D simulation base case.

There will be no modifications done to the Spalart Allmaras turbulence model considering the development of laminar separation bubbles.

Simulation of 3D single- and co-axial rotor

This chapter is the is going to explain choices made when simulating the single- and co- axial rotor configuration. Turbulence model validated in 2D simulation of a airfoil is going to be used without modifications. While the grid generation part of the 3D simulations will undergo the same process of determining grid as the 2D simulations.

To verify the result of the 3D simulation, the experimental values from UiS laboratory will be used for comparison. The experimental values are gathered using a test rig of a coaxial rotor thrust stand controlled by RCBenchmark. RCBenchmark lets the operator control the change in % of throttle input, and provides information of torque, thrust, voltage, ampere, motor optical speed and a mechanical power usage. The experimental results have been validated using the engine providers test report with same propeller and voltage. Since the experimental data includes a wide range of RPM (motor optical speed) values, a specific RPM values is easily compared. The RPM value used in calculations for Reynolds number and propeller velocities in table 3.4 is going to be used in the 3D simulations.

5.1   3D - Single Rotor simulations

The initial grid and solver setting will be as similar to the 2D validation case as possible. Although a similar, but transient solver is required for a dynamic mesh. Pimple instead of SIMPLE will be used in 3D simulations.

The rotational velocity as initial velocity will be similar to the rotational speed of the standard rotor setup which Nordic Unmanned is using today at hoover, see table 3.4. Using 2000 RPM as initial velocity requires and AMI moving the propeller with a rotational speed of 210 rad/s. AMI stands for

Table 5.1: Initial Grid

Domain thickness	8 m
Refinement level 0 thickness	0.05 m
y+, calculated first layer thickness	6.211 e-6 m
Highest refinement level	7
Highest refinement level thickness	3.905 e-4 m
Relative size parameter	0.5
Final layer thickness	1.953 e-4 m
Expansion ratio	1.3
Number of Surface Layer	15
Final layer thickness	4.960 e-6 m

Arbitrary Mesh Interface, and is used when simulating rotating geometries, where there is a moving- and a stationary part. The AMI should be placed around the propeller, small enough to not interfere with the AMI placed around the lower propeller in a coaxial setup.

In order to increase flight endurance, a co axial propeller configuration optimized for operating in the International Standard Metric Conditions with relations to pressure and temperature.

The initial axial separation will be standard distance between mounted propeller of 109.2 mm with a small adjustment for propeller width leaving the initial axial separation at z0 = 115 mm.

5.1.1   Computational Setup

Performing the same process for the 3D simulations to determining grid size and refinement as preformed for the 2D simulations to provide table 4.1.

The domain length and width are set at 20 times propeller radi, calculating y+ < 1 equals a first layer thickness of 6.211e-6 m generates table 5.1.

Implementing values given by table 5.1 results in grid refinement levels and surface layer shown in figure 5.1.1 and 4.1.1. After 0.1 s, both Torque and Thrust converge. Torque is multiplied with rotational speed [rad/s] in order to display power usage [W]. Comparing the thrust, torque and power values with the experimental values can be inspected in table **??** along with three different level of grid refinements. From the grid refinement/ independece study, see table 4.1.1, it's clear that an increase in grid refinement has the most impact on y+ and computational time, and that Thrust, and Torque have minimal variations. Going forward, the medium grid refinement is going to be used since it provides reasonable y+ values in reasonable time, and there are no significant changes in thrust and torque increasing the grid refinement
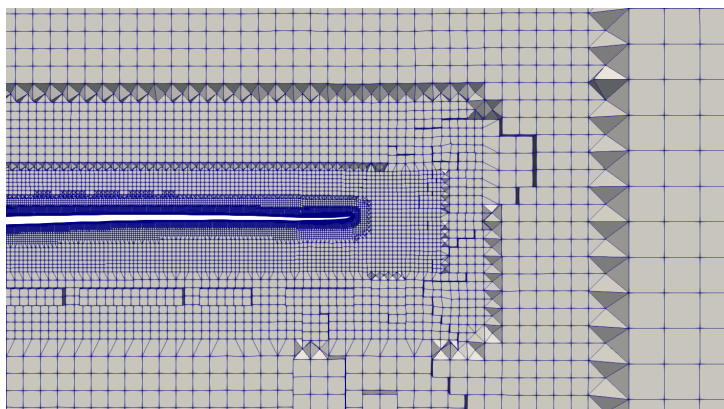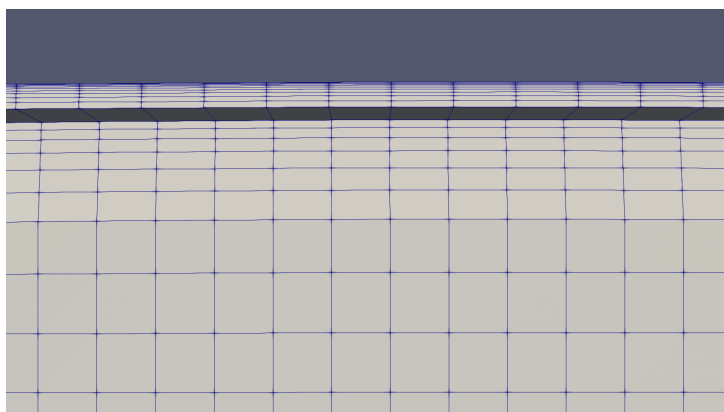
Figure 5.1: Grid refinement Level

Figure 5.2: Surface Layer transition

to fine. Table 5.2 also includes the experimental values of the same propeller size rotating at the same velocity. 24 N to 16 N are clearly not accurate enough, and a few options of providing better result should be implemented. Since the gridd refinement didn't not improve the accuracy of the results, verify the accuracy of the 3D mode and check if a different solver approach for velocity and/or pressure provides more accurate results could help improve the accuracy of the results. Although, the grid refinement/ independence study proves that the inaccurate values are not grid dependent.

5.1.2 Results Single rotor Simulations

In this subsection every results regrading Single rotor simulations will be documented. In addition to the result, an attempt to explain the result accompanied by using OpenFOAM post processing tool Para-View to visualize

Table 5.2: Grid Refinement for Single 28" Propeller

	28S Coarse	28S Medium	28S Fine	Exp. Values
y+ Propeller	2.392	1.877	1.317	
nCells	4,247,427	6,123,401	8,730,655	
cTime [s]	60,748	127,786	175,277	
Thrust [N]	15.902	16.181	16.338	24.358
Torque [Nm]	0.544	0.544	0.544	0.808
Power [W]	113.867	113.960	113.894	171.059

the explanation. All figures are either created using plots from simulation data or graphical representations using Para-view.

Single Rotor Comparison same RPM

In table 3.4, an estimated RPM of 2000 for the 28"x9.2" propeller needed to almost provide high enough thrust for BG-200 to hover for the smallest propeller. The smaller sized propellers will not provide sufficient lift at 2000 RPM to counter gravitational effects, while the larger sized propeller at 2000 RPM will provide an positive vertical acceleration. Comparing thrust, power and efficiency for all Single Rotor at 2000 RPM are plotted in figure 5.1.2, 5.1.2 and 5.1.2. Figure 5.1.2 is each individual propellers thrust divided with power usage. Power is calculated from torque times rotational velocity (rad/s). Figures 5.1.2, From figure 5.1.2 using single rotor of 28"x9.2" is
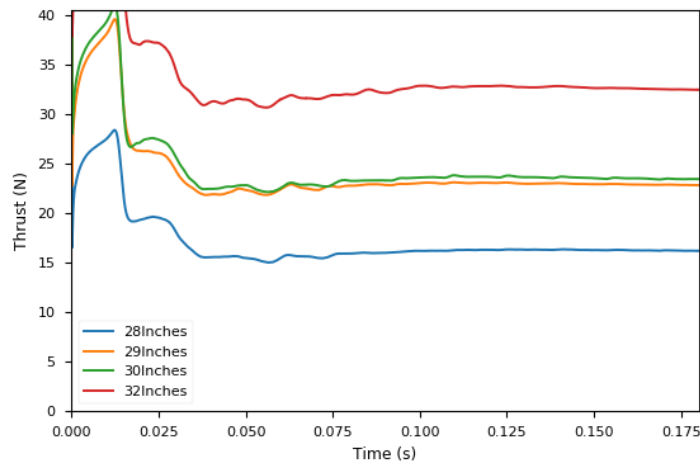

Figure 5.3: Single Rotor Thrust

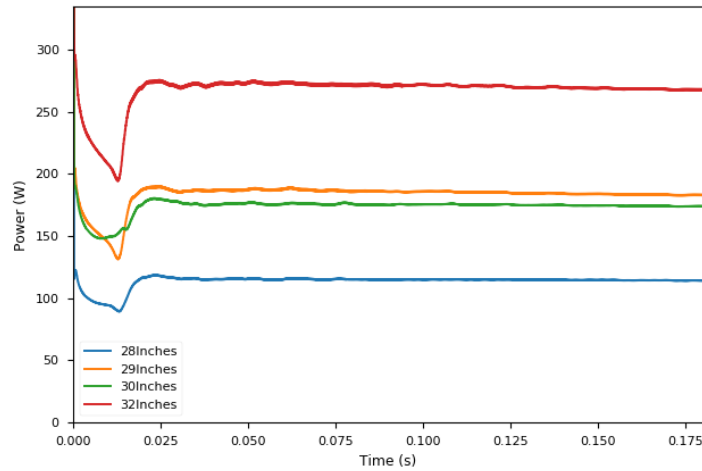the most efficient compared to the larger propellers, all operating at 2000
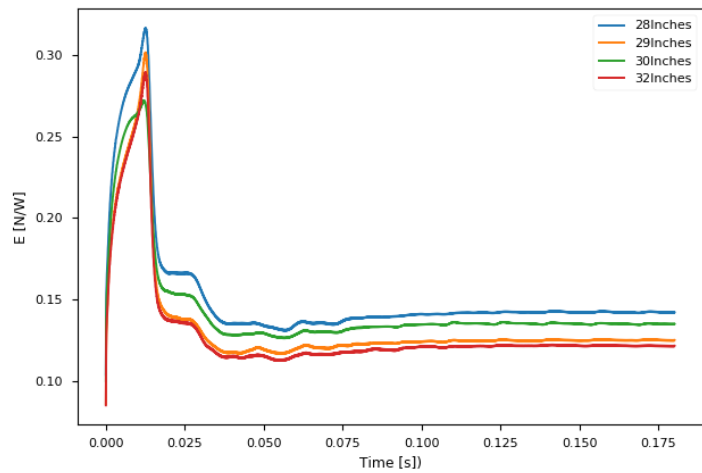
Figure 5.4: Single Rotor Power

Figure 5.5: Efficiency Single Rotor

RPM. The efficiency of 30"x10.5" among values from figures 5.1.2 and 5.1.2 suggest there is something wrong with the 3D models. Inaccurate 3D models can also explain the thrust and torque difference encountered during grid Independence study. Table 5.3 includes the stl. files with error % , compared to experimental values of thrust and torque, where $thurst_e$ and $torque_e$ is the experimental values at 2000 RPM. In order to utilize the accuracy of 3D model 29"x9.5", 29"x9.5" is scaled to match the same radius as the other propeller. 29"x9.5" was the most accurate 3D model, and is scaled at 0.9673, 1.0000, 1.0381, 1.1117 in x, y and z direction, representing the smallest to

largest propeller.

Looking at the increased accuracy of the scaled propeller compared to

Table 5.3: 3D model accuracy at 2000 RPM

Propeller	Thrust [N]	$Thrust_e$ [N]	[%]	Torque [Nm]	$Torque_e$ [Nm]	[%]
28" 9.2"	16.18	24.36	0.66	0.544	0.808	0.67
29" 9.5"	22.8	26.9	0.85	0.87	0.94	0.93
30" 10.5"	23.4	34.6	0.68	0.86	1.26	0.68
32" 11"	32.5	41.1	0.79	1.28	1.57	0.82

the experimental result, the scaled propeller will be used when comparing different sized propeller when it seems more likely to provide a more realistic result. All simulations will not be rerun using scaled propellers, but only highlighted when scaled propellers are used.

RPM range

When looking into change in efficiency at different RPM, the original propeller stl. are being used. Table 5.4 shows propeller 32"x11" at three different rotational velocity, 1700, 1850 and 2000 RPM. Table 5.4 shows an increasing

Table 5.4: Different Rotational Velocity

RPM	1700	1850	2000
Thrust [N]	23.2144	27.6615	32.4919
Torque [Nm]	0.9167	1.0897	1.2775
Power [W]	163.2030	211.1045	267.5636
Efficiency [N/W]	0.1422	0.1310	0.1214

efficiency when lowering rotational velocity. The ratio of increase between thurst with an increase in RPM is slight lower than the ratio of increase in torque. Figure 5.1.2 and figure 5.1.2 shows the difference in velocity magnitude in the domain directly above a single rotor propeller operating at 1700 and 2000 RPM. These indicate that the higher rotational velocity have an increased blade to blade interference. This is reducing the relative rotational speed in the rotational plane, while the increase in inflow is stable. Reducing the potential increase in thrust, while maintaining the increase in torque when increasing rotational speed.
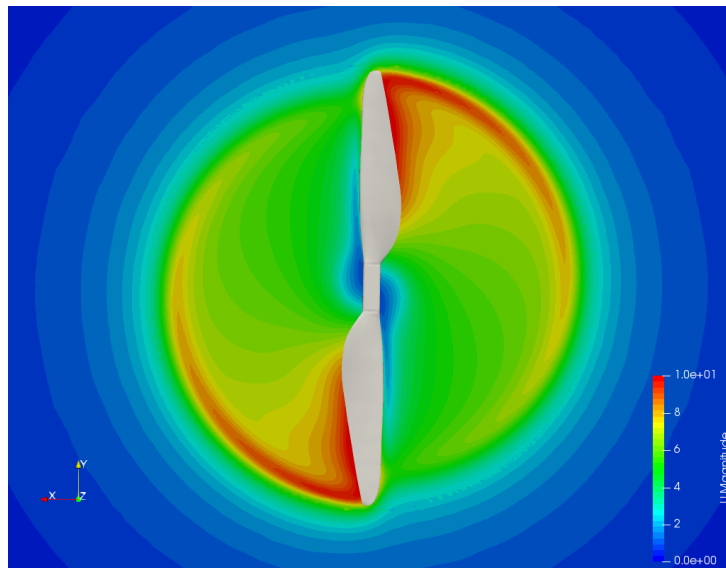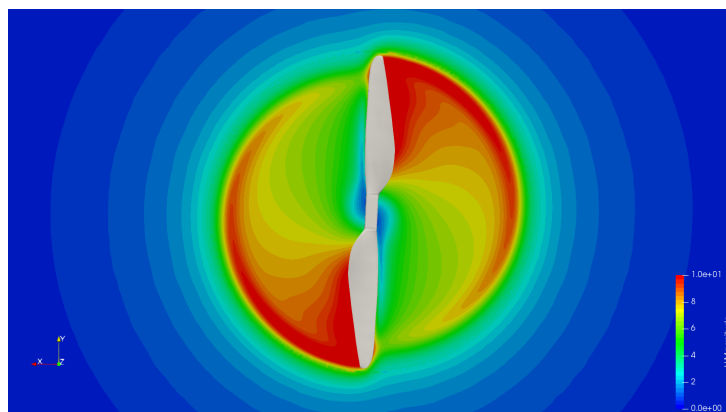
Figure 5.6: U 32" at 1700 RPM

Figure 5.7: U 32" at 2000 RPM

Single Rotor, same weight comparison

To accurately compare the single rotor, an comparison where the different sized propellers provide the same amount of torque is provided in table 5.5. Looking at table 5.5, the propeller operating at the lowest RPM is clearly the most efficient in terms of thrust per watts. The increase in efficiency from 28" to 30" seems to be an increase of 0.01, but from 30" to 32" only 0.005. This suggest that the efficiency gain from reducing rotational velocity is not linear.

Table 5.5: Single Rotor Comparison, similar upward thrust

Propeller	28x9.2(Scaled)	29x9.5	30x10.5(Scaled)	32x11(Scaled)
RPM	2265	2050	1855	1670
Thrust [N]	25.4404	23.9292	22.7628	24.3455
Torque [Nm]	0.9429	0.9164	0.8988	1.0323
Power [W]	223.6413	196.7198	174.5913	180.5307
Efficiency [N/W]	0.1138	0.1216	0.1304	0.1349

5.2   3D - Co-Axial Rotor simulations

Determining the most efficient single rotor propeller as G32"x11" from 3D - Single Rotor Simulations will be explored further in this chapter in co axial setups. Unmanned standard setup of using G28"x9.2" as both Upper and Lower propeller will be compared against several of options implementing the use of G32"x11" as well as tested at different axial separation to determine if different propeller combinations or axial separation provide efficiency gains in terms of flight endurance.

5.2.1   Computational Setup

There isn't much difference between the computational setup of 3D single and 3D co-axial rotor simulations. In order to create a contra rotating co axial rotor setup an additional AMI has been placed around the Lower propeller with the exact refinement levels used as in the AMI of the upper/single rotor propeller rotating CW instead of CCW. Since the additional AMI is a copy of the AMI used in single rotor setup, there will not be an additional grid Independence study for the coaxial rotor setup. The finished grid of the co-axial rotor setup can be seen in figure 5.2.1.

5.2.2   Results Co- axial simulations

In this subsection every result regarding co- axial rotor simulations will be documented. In co- axial result compared to the single Rotor result, the same thrust will be presented directly. The axial separation of the co- axial simulation only include data from a co axial rotor setup with G28"x9.2" as both upper and lower propeller.
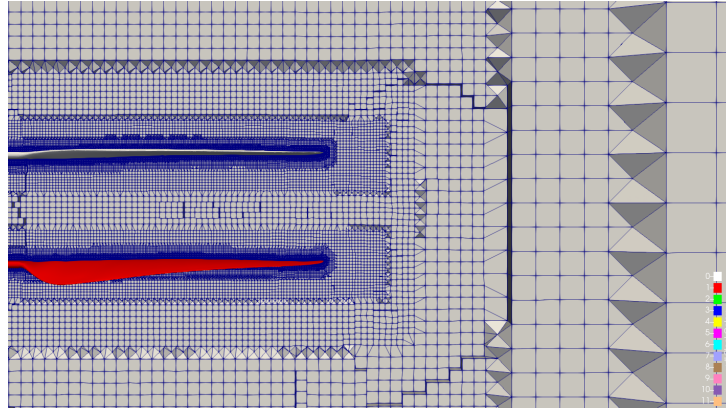
Figure 5.8: Finished Grid Co Axial

Co-axial rotor comparison same weight

Experimental data from UiS labratory is available for standard co axial rotor setup and given in table 3.3. This data provides combined 40.2 N. All co axial simulations in table 5.6 have been a adjusted with 200 RPM in order to provide about the same upward thrust as the experimental values. The

Table 5.6: Co-Axial rotor Comparison, same upward thrust

Thrust [N]	Upper	Lower	Combined
U28 L28	24.3974	16.5092	40.9066
U28 L32	18.4611	24.5950	43.0561
U32 L32	23.8808	16.3850	40.2658
Torque [Nm]			
U28 L28	0.9835	0.8507	1.8342
U28 L32	0.7376	1.2206	1.9582
U32 L32	1.0828	0.9585	2.0413
Efficiency [N/W]			
U28 L28	0.1150	0.0900	0.1034
U28 L32	0.1343	**0.1159**	0.1231
U32 L32	0.1404	0.1088	**0.1256**

upper propeller in these rotor setups are all acting as an isolated Single rotor, see table 5.6, the difference of U28 L32 and U28 L28 for the upper propeller is because of reduction in rotational velocity by the increased contribution of the lower 32" propeller. And as witnessed in Single Rotor same thrust subsection, the most efficient upper propeller is the largest propeller operating with the lowest rotational speed.

The lower propeller, operating in the slipstream of the upper propeller, has it's highest efficiency when the upper propeller has a smaller diameter. The lift distribution of the propeller can be seen in figure 5.2.2 and a small scale increase of the lower propeller can increase the high lift areas not effected by the slipstream of the upper propeller. See figure 5.2.2 of standard setup, and how the slipstream of the upper propeller effects the lower propeller. The
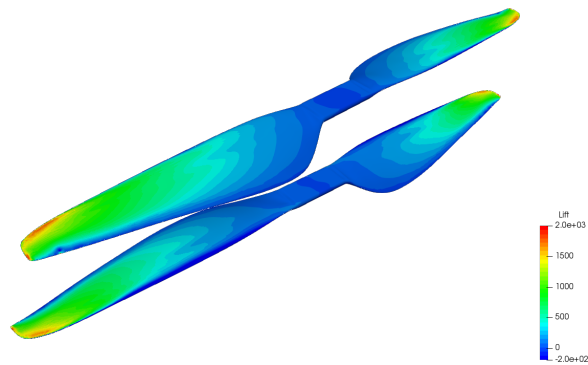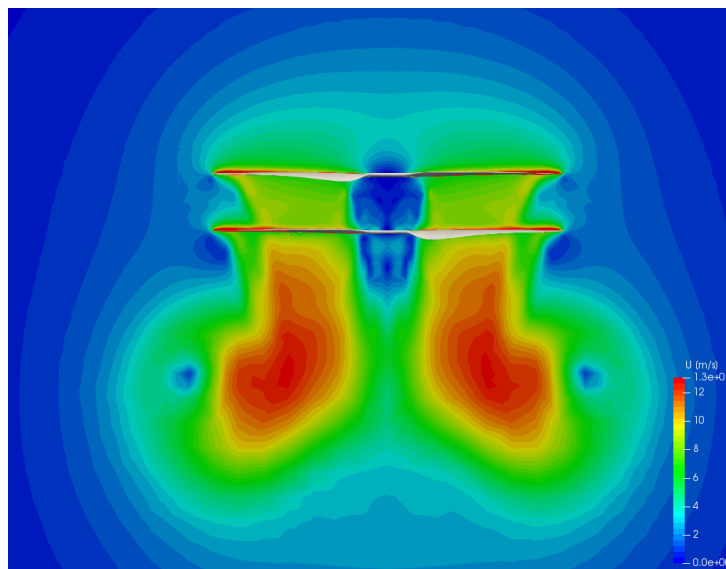

Figure 5.9: Lift Distribution

Figure 5.10: Slipstream in a standard setup

combination of the inflow of the lower propeller and the slipstream of the upper propeller effects the relative rotational velocity of the lower propeller.

Pressure field taken from simulation of the standard setup, see 5.2.2, shows a pressure concentration at the leading edge of the upper propeller, where the relative wind first connects with the airfoil. The leading edge is shifted upwards on the lower propeller, reducing the curving of the streamlines, lower the magnitude of the low pressure above the airfoil and reducing lift contribution of the lower propeller. Still, with the increase of efficiency of the lower
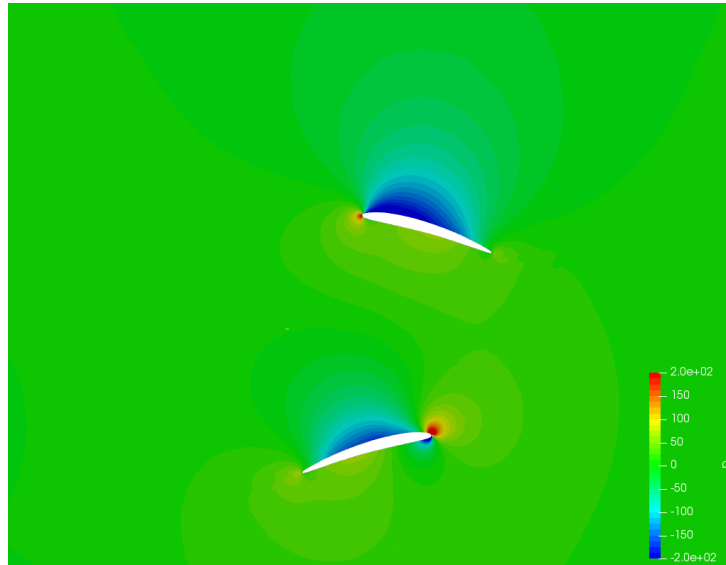

Figure 5.11: Pressure Field of a standard setup

propeller in a different scaled propeller setup. The overall efficiency of the rotor configuration utilizing two 32" propellers operating at low rotational velocity is the most efficient, with a added increase in torque to the standard setup.

Co-axial rotor axial separation

The BG-200 is designed to the 28" propellers, geometry and engine wise. This subsection will therefore test the standard setup and determine the efficiency gain and loss at different axial rotor separation to the standard setup.

Axial separation, z/D, where z is axial separation and D is the diameter of the upper propeller. In this case (G28"x9.2" propeller), 0.16-, 0.2-, 0.3- and 0.4 z/D measures 115-, 142-, 215- and 285 mm axial separation. Values from simulations testing axial separation can be found in table 5.7. At an axial separation of $0.2z/D$ an efficency increase of upper propeller is similar

Table 5.7: Co-Axial rotor Comparison, Axial Separation

z/D	0.16	0.2	0.3	0.4
Thrust [N]				
Upper	23.1124	24.2693	24.4495	24.3920
Lower	11.8517	16.7616	16.3948	16.0788
Combined	34.9641	41.0309	40.8443	40.4708
Power [Nm]				
Upper	195.9531	195.4726	193.6002	192.0744
Lower	152.4137	172.1032	170.3275	172.6963
Combined	348.3668	367.5758	363.9277	364.7707
Efficiency [N/W]				
Upper	0.1190	0.1242	0.1263	0.1270
Lower	0.0778	0.0974	0.0963	0.0931
Combined	0.1004	0.1116	**0.1120**	0.1109

to the effiency decrease of the lower propeller leaving the overall effiency
minimal. The higest efficiency gain is from increasing axial separation from
0.16 z/D to 0.2 z/D, because of the significant efficiency loss of the otherwise
most efficienct propeller in the co - axial rotor setup. These findings correlate
with studies done by Brazinskas et al, where they studied co axial setup of
T- Motors P16"x5.2" propeller [3].

5.2.3 Flight Endurance

Unmanned Nordic are using two 28"x9.2" propeller in each co axial setup
of their octocopter. In an attempt to maximize their flight endurance, this
thesis have been looking into the efficiency benefits of, replacing one or both
of the propeller in each of the co axial rotor configuration, and how different
axial separation of the propellers impact the overall flight endurance. A
simplified measure of gains in flight endurance, without taking height of
motor efficiency is given in equation 5.1.

$$\text{Flight endurance}_s \frac{\text{Combined Efficiency}_p}{\text{Combined Efficiency}_s} = \text{Flight endurance}_p \qquad (5.1)$$

From table 5.6, a change of lower propeller from standard 28" to 32" will
have a potential increase in flight endurance of:

$$60 \text{ min} \frac{0.1231}{0.1034} = 71.4 \text{ min} \qquad (5.2)$$

Chaning both propellers to 32" and utilizing the most efficienct co - axial setup studied in this thesis have a potential increase in flight endurance of:

$$60 \text{ min } \frac{0.1256}{0.1034} = 72.9 \text{ min} \tag{5.3}$$

From table 5.7, the combined efficiency of axial separation of 0.3 z/D is 0.1120 N/W which is an increase of 0.116 from standard setup considering 40 N, will give a potential increase in flight endurance of:

$$60 \text{ min } \frac{0.1120}{0.1004} = 66.9 \text{ min} \tag{5.4}$$

Conclusion

In this thesis, a co axial propeller configuration optimization study has been made of four different propellers at four different axial separation distances. Computational Fluid Dynamics simulations of 3D co-axial rotor simulation, 3D single rotor simulation and 2D airfoil simulation was completed using OpenFOAM. The 2D airfoil simulation was used to validate the turbulence model and grid Independence study used in both 3D simulations.

3D simulation of the single rotor cases was completed in order to determine the efficiency of each propeller individually. Only the most efficient propeller was compared to the standard setup, to verify the propeller combination efficiency. Every propeller combination was tested to determine which co- axial rotor configuration provided the highest possible flight endurance.

Results revealed that the co axial propeller setup which provided thrust equal to the one forth of the total weight demand, was the propeller operating at the lowest rotational velocity. The importance of controlling rotational velocity because of blade to blade interference is crucial when optimizing co-axial propeller configuration for flight endurance.

Changing the standard setup of two 28"x9.2" propeller with two 32"x11" propeller increased to theoretical flight endurance at zero payload from 60 min to 72.9 min, while only chancing the lower propeller with a 32"x11" propeller still provided 11.4 min.

The highest efficiency gain on the lower propeller was found when using a small upper, and larger lower propeller, because of minimizing the effect of the slipstream of the upper propeller.

Different axial separation simulations showed that an increase of axial separation from 0.16 z/D to 0.2 z/D had a positive effect on efficiency. Further increasing the axial separation showed minimal gains in terms of efficiency, but the entire range from 0.2 to 0.4 seemed fairly stable. A standard setup with increased axial separation to 0.3 z/D will provide an efficiency gain to the standard 0.16 z/D which account for fluctuations in rotational velocity. The potential increase in flight endurance at zero payload with axial

separation of 0.3 z/D is about 67 min.

6.1 Computational Fluid Dynamics

CFD analysis of fluid problems is numerical approximation of the actual fluid problems. Increasing the accuracy of a CFD simulation can be achieved by increasing grid refinement, fully develop surface layer and select higher order and more accurate discretisation schemes. Every improvement comes with a increased computational costs, and a selection between available time and computational power against simulation accuracy must be made.

CFD simulations in this thesis have good agreement with the experimental results from UiS machine laboratory, but with low accuracy. This provides an opportunity to run more experiments at a lower accuracy, while still obtaining simulations with good agreement.

With the development of computer- hardware and software, and the continues increase in computational power, some of the present options made to reduce computational time will be neglected. This will potentially lower the requirements to the CFD designer and increase the overall accuracy of CFD simulations. Making the performance of this thesis a wonderful step into the world of CFD.

6.2 Further Work

This section is a quick run through of potential areas of study or improvements that have been encountered throughout this thesis.

Increased accuracy of simulations

All 3D models accuracy should be tested using CMM, to verify and improve the inaccuracy of the simulations. All 3D models is also infinitely stiff, and might provide more realistic results being elastic. Secondly, recreating the simulation files and choose more accurate discreatisation schemes, while still being stable and a fully developed surface layer around the wing tips.

More simulations

A wider range of simulations in the axial separation study an additional simulations testing different propeller combinations. Testing different propeller combinations should also be included in the co - axial rotor comparison study,

especially 29", which Nordic Unmanned already cleared for use at lower rotational velocities. Modifications done to the geometry and inlet condition can easily be tested using small adjustments to the present simulations files. Modifications such as, inlet velocity, co rotating propeller study, increased number of blades, and optimize the design of the lower propeller would be interesting to simulate when looking at the potential in increased flight endurance.

References

[1] *Taking flight*, Library Catalog: www.economist.com. [Online]. Available: `http://www.economist.com/technology-quarterly/2017-06-08/civilian-drones` (visited on 05/06/2020).

[2] *Nordic Unmanned - One of the leading drone service provider in Europe*, en-US, Library Catalog: nordicunmanned.com. [Online]. Available: `https://nordicunmanned.com/about/` (visited on 05/05/2020).

[3] M. Brazinskas, S. Prior, and J. Scanlan, "An Empirical Study of Overlapping Rotor Interference for a Small Unmanned Aircraft Propulsion System", en, *Aerospace*, vol. 3, no. 4, p. 32, Oct. 2016, ISSN: 2226-4310. DOI: `10.3390/aerospace3040032`. [Online]. Available: `http://www.mdpi.com/2226-4310/3/4/32` (visited on 05/05/2020).

[4] S. D. Prior, "Reviewing and Investigating the Use of Co-Axial Rotor Systems in Small UAVs", en, *International Journal of Micro Air Vehicles*, vol. 2, no. 1, pp. 1–16, Mar. 2010, ISSN: 1756-8293, 1756-8307. DOI: `10.1260/1756-8293.2.1.1`. [Online]. Available: `http://journals.sagepub.com/doi/10.1260/1756-8293.2.1.1` (visited on 05/05/2020).

[5] S. Walker, "Langley Research Center Hampton, Virginia", en, p. 234,

[6] P. R. Spalart and C. L. Rumsey, "Turbulence Model Behavior in Low Reynolds Number Regions of Aerodynamic Flowfields", eng, 2008. [Online]. Available: `http://ntrs.nasa.gov/search.jsp?R=20090017753` (visited on 06/23/2020).

[7] J. G. Leishman and S. Ananthan, "AERODYNAMIC OPTIMIZATION OF A COAXIAL PROPROTOR", en, p. 23,

[8] Yunus A. Çengel, *Fluid mechanics: fundamentals and applications*, eng, 3rd ed. in SI units. Boston: McGraw-Hill, 2014, Pages: XXIV, 986, ISBN: 978-1-259-01122-1.

[9]   H. K. Versteeg, *An introduction to computational fluid dynamics: the fi-nite volume method*, eng, 2nd ed. Harlow: Pearson/Prentice Hall, 2007, Pages: XII, 503, ISBN: 978-0-13-127498-3.

[10] P. Spalart and S. Allmaras, "A One-Equation Turbulence Model for Aerodynamic Flows", *AIAA*, vol. 439, Jan. 1992. DOI: `10.2514/6.1992-439`.

[11] J. Morgado, R. Vizinho, M. Silvestre, and J. Páscoa, "XFOIL vs CFD performance predictions for high lift low Reynolds number airfoils", en, *Aerospace Science and Technology*, vol. 52, pp. 207–214, May 2016, ISSN: 12709638. DOI: `10.1016/j.ast.2016.02.031`. [Online]. Available: `https://linkinghub.elsevier.com/retrieve/pii/S1270963816300839` (visited on 05/05/2020).

[12] OpenCFD, *Numerical schemes*, en, Library Catalog: www.openfoam.com. [Online]. Available: `http://www.openfoam.com` (visited on 06/24/2020).

[13] J. Nobrega and H. Jasak, Eds., *OpenFOAM® : Selected Papers of the 11th Workshop*, en. Springer International Publishing, 2019, ISBN: 978-3-319-60845-7. DOI: `10.1007/978-3-319-60846-4`. [Online]. Available: `https://www.springer.com/gp/book/9783319608457` (visited on 06/14/2020).

[14] M. Tomislav, *The OpenFOAM Technology Primer*. Sourceflux, 2014, ISBN: 978-3-00-046757-8.

[15] *STAAKER BG200 - Nordicunmanned - Leading European Provider*, en-US, Library Catalog: nordicunmanned.com, Dec. 2019. [Online]. Available: `https://nordicunmanned.com/products/unmanned-systems-drones/staaker-bg200/` (visited on 05/19/2020).

[16] Mikell P. Groover, *Automation, production systems, and computer-integrated manufacturing*, eng, 3rd ed. Upper Saddle River, N.J: Pearson Prentice-Hall, 2008, Pages: XVI, 815, ISBN: 978-0-13-239321-8.

[17] Creaform, *HandySCAN 3D Scanner for 3D Metrology*, en, Library Catalog: www.creaform3d.com. [Online]. Available: `https://www.creaform3d.com/en/portable-3d-scanner-handyscan-3d/technical-specifications` (visited on 06/14/2020).

[18] *2D NACA 4412 Airfoil Trailing Edge Separation*. [Online]. Available: `https://turbmodels.larc.nasa.gov/naca4412sep_val.html` (visited on 06/14/2020).

[19] D. C. Jespersen, T. H. Pulliam, and M. L. Childs, "OVERFLOW Turbulence Modeling Resource Validation Results", en, p. 176,